MINISTRY OF EDUCATION AND TRAINING

VIETNAM ACADEMY OF SCIENCE AND TECHNOLOGY

GRADUATE UNIVERSITY OF SCIENCE AND TECHNOLOGY

---------📖---------

NGUYEN BA MANH

SYNTHESIS OF MATERIALS BASED ON THE Me-BTC METAL-ORGANIC FRAMEWORK FOR APPLICATION IN THE TREATMENT OF TETRACYCLINE RESIDUES AND ADSORPTION OF H_2S AND CO_2 GAS

SUMMARY OF DISSERTATION ON SCIENCES OF MATTER

Major: Theoretical Chemistry and Physical Chemistry

Code: 9.44.01.19

Ha Noi – 2025

The dissertation is completed at: Graduate University of Science and Technology, Vietnam Academy Science and Technology

Supervisors:

1. Supervisor 1: Assoc.Prof. Dr. Doan Le Hoang Tan, Ho Chi Minh City National University
2. Supervisor 2: Dr. Pham Thi Lan - Institute of Materials Science

Referee 1: Prof. Dr. Vu Thi Thu Ha

Referee 2: Dr. Tran Quang Vinh

The dissertation is examined by Examination Board of Graduate University of Science and Technology, Vietnam Academy of Science and Technology at 9: 00 a.m (date 14 November 2025)

The dissertation can be found at:

1. Graduate University of Science and Technology Library
2. National Library of Vietnam

INTRODUCTION

1. 1. Urgency of the thesis

Currently, the air quality in major cities is being seriously polluted due to the emissions gases such as CO, CO_2, H_2S, SO_x, NO_x and fine dust (PM10, PM2.5) exceeding regulatory limits. Many countries have been increasing the use of cleaner, greener energy sources to reduce the emission of air pollutants such as solar energy, wind energy, liquefied petroleum gas (LPG), or compressed natural gas (CNG). Among them, CNG, mainly composed of methane, can reduce emissions by up to 70% compared to conventional gasoline engines. However, to make CNG cleaner and greener, the prerequisite is to "sweeten" it through the removal of acid gases like CO_2 and H_2S. CO_2 and especially H_2S in natural gas can be cause catalysts poisons, causing equipment corrosion and significantly impacting operational processes. Among the methods used, the adsorption of acidic gases by metal-organic frameworks (MOFs) possess a high specific surface area, large pore volume, and particularly suitable pore sizes for gas adsorption under ambient conditions. Among the MOF materials, Me-BTC is considered to have the best CO_2 adsorption capacity under ambient conditions, as Me-BTC has pore sizes including tetrahedral channels (5 Å) and square channels (9 Å) that are close to the kinetic diameter of acidic gases, thereby enhancing the ability to adsorb acidic gases under environmental conditions. However, Me-BTC is not stable in high humidity environments, limiting practical applications because water vapor molecules can attack the metal-oxygen coordination sites, leading to the destruction of the Me-BTC structure.

Another issue that domestic researchers are particularly concerned about is the serious water pollution caused by residual antibiotics. Because antibiotics are not treated or inadequately treated before being discharged into the water environment, they pollute groundwater, rivers, lakes, seas, and can enter the food chain. Antibiotics in water can lead to the formation

and development of antibiotic-resistant bacterial strains, threatening the effectiveness of antibiotic treatment for humans and disrupting the ecological balance. Antibiotics in water are very persistent and stable, making them difficult to separate through filtration or biological degradation methods. Photocatalytic technology in treating harmful organic substances like residual antibiotics is considered an environmentally friendly method, causing no secondary pollution, recyclable, effective, highly selective with low cost, and easy to operate. However, typical photocatalysts often have high bandgap energy, low specific surface area, and unstable activity. To overcome these drawbacks, Z-Scheme photo-catalysts have been synthesized with many superior advantages compared to traditional p-n type photocatalysts such as (i) simultaneously preserving the reducing and oxidizing properties of semiconductors, (ii) expanding the visible light absorption capability; (iii) efficient charge separation and hole trapping; (iv) inhibiting the recombination of photo-generated electrons and holes; (v) shortening the charge transport distance due to the dual charge transfer process. Indeed, metal-organic framework materials based on Me-BTC are modified with semiconductors such as Ag_3PO_4, GCN, ZnO, TiO_2, ... to form Z-Scheme photocatalysts that exhibit superior antibiotic treatment efficiency. However, Z-Scheme semiconductor materials still have the disadvantage of limited charge separation and transmission due to the interaction of loosely bound semiconductor phases. In addition, Me-BTC is often synthesized with toxic solvents, high costs, environmental pollution such as methanol (MeOH), dimethylformamide (DMF), for a long synthesis time (24-72 hours) and at high temperatures (150-200 ^oC). Therefore, this study aims to create durable Me-BTC materials in a high humidity environment, without using toxic organic solvents, reducing crystallization time, applying for acid gas adsorption. Furthermore, Me-BTC is modified with GCN and Ag_3PO_4 combined with carbon quantum dots (CQD) to enhance binding, transmission, and electron separation

capabilities, applied in DLKS treatment. Therefore, the topic "Synthesis of materials based on the Me-BTC metal-organic framework for application in the treatment of tetracycline residues and adsorption of H_2S and CO_2 gas" is of high practical scientific significance.

THE RESEARCH OBJECTIVES OF THE THESIS

Synthesize composite GCN/Me-BTC (Me: Fe, Cr, Cu, Co, Mn, and Ni), GCN/FeNi-BTC/CQD, Ag_3PO_4/GCN/FeNi-BTC/CQD for efficient photo-catalytic degradation of tetracycline antibiotics in water.

Synthesize M-Cu-BTC-II materials (M: Mg, Fe, Ni, Co, Mn, Zn, and Zr; II: isopropanol and imidazole) for highly effective adsorption of acid gases (CO_2 and H_2S).

RESEARCH CONTENT OF THE THESIS

Research on the synthesis and characterization of GCN/Me-BTC materials (Me: Fe, Cu, Ni, Co, Mn, and Cr), GCN/FeNi-BTC/CQD, Ag_3PO_4/GCN/FeNi-BTC/CQD (AGF-CQD) and M-Cu-BTC (M = Mg, Fe, Ni, Co, Cu, Mn, Zn, and Zr) using a combination of hydrothermal and microwave methods.

RESEARCH CONTENT OF THE THESIS

The research synthesizes and characterizes GCN/Me-BTC materials (Me: Fe, Cu, Ni, Co, Mn, and Cr), GCN/FeNi-BTC/CQD, Ag_3PO_4/ GCN/ FeNi-BTC/CQD (AGF-CQD), and M-Cu-BTC (M = Mg, Fe, Ni, Co, Cu, Mn, Zn, and Zr) using a combination of hydrothermal and microwave methods.

The study evaluates the ability to degrade the antibiotic tetracycline in water environment of the synthesized materials. Researching factors affecting the efficiency of the photocatalytic process such as initial tetracycline antibiotic concentration, pH, and catalyst mass. Assessing the roles of reaction radicals such as h^+, $^{\bullet}O_2^-$, and $^{\bullet}OH$, based on electrochemical analysis and the role of reaction radicals, studying the construction of material band structures.

Evaluating the ability to adsorb CO_2, H_2S, CH_4, N_2 gases of the M-Cu-BTC-II material and the influence of temperature on the adsorption capacity of CO_2, H_2S gases. Proposing reaction mechanisms and evaluating the stability of CO_2 gas adsorption after different cycles.

STRUCTURE OF THE THESIS

The thesis consists of 132 pages, 97 Figures, 28 Tables, and 222 references. The structure of the thesis includes the following parts: introduction, 3 content chapters, and conclusion. The new contributions of the thesis are published in 04 reputable articles in SCIE (Q1) Journals.

CHAPTER 1. OVERVIEW

Chapter 1 is presented in 30 pages, introducing an overview of photocatalysts Z-scheme, MOF applied in water and air environmental treatment, synthesis of MOF by hydrothermal method combined with microwave, material systems Ag_3PO_4, GCN, CQD, Fe-BTC, and Cu-BTC.

CHAPTER 2. EXPERIMENT

Chapter 2 is presented in 14 pages including:

2.1. Chemicals and equipment

2.2. Experimental synthesis process of materials

Synthesis process of materials GCN, CQD, and Ag_3PO_4

Synthesis process of GCN/Me-BTC (Me: Fe, Cu, Ni, Co, Mn, and Cr)

Synthesis process of materials GCN/CQD/FeNi-BTC

Synthesis process of Ag_3PO_4/GCN/FeNi-BTC/CQD (AGF-CQD)

Synthesis process of materials Cu-BTC-II and M-Cu-BTC-II

2.3. Characterization methods of materials

Characterization of physicochemical properties of materials including XRD, FTIR, EDS, XPS, BET, SEM, TEM, electrochemical methods (UV-Vis DRS, PL, Photocurrent, Mott-Schottky, EPR, and EIS).

2.5. Evaluation of material efficiency

Evaluation of the activity of materials GCN, CQD, Ag_3PO_4, GCN/Me-BTC, GCN/CQD/FeNi-BTC, Ag_3PO_4/GCN/FeNi-BTC/CQD in the process of treating antibiotic tetracycline in water environment.

Evaluation of the adsorption capacity of gases CO_2, H_2S, CH_4, N_2 of material M-Cu-BTC-II and the influence of temperature on the adsorption capacity of gases CO_2, H_2S.

CHAPTER 3. RESULTS AND DISCUSSION

Chapter 3 is presented in 84 pages

3.1. Characteristics and applications of GCN/Me-BTC in tetracycline treatment and CO_2 adsorption.

3.1.1. Characteristic results of GCN/Me-BTC materials

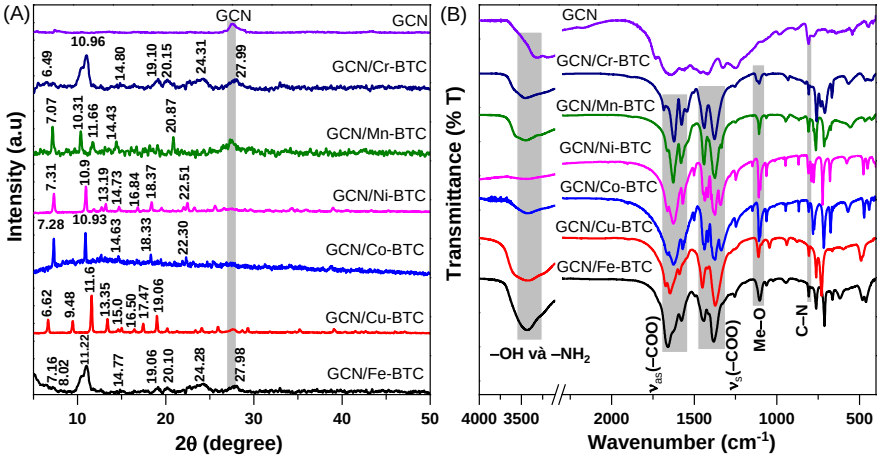

Figure 3.1. XRD patterns (A) and FTIR spectra (B) of GCN and GCN/Me-BTC materials

The X-ray diffraction (XRD) patterns of GCN and GCN/Me-BTC materials are presented in Figure 3.1A. The XRD pattern of GCN/Fe-BTC material shows peaks at 2θ of 7.16°, 8.02°, 10.96°, 11.22°, 14.77°, 19.06°, 20.10°, 24.28°, and 27.98° characteristic of the Fe-BTC phase [108]. The GCN/Cu-BTC material exhibits peaks at 2θ of 6.62°, 9.48°, 11.60°, 13.35°, 15.0°, 16.50°, 17.47°, and 19.06° characteristic of the Cu-BTC phase [111].

Peaks at 2θ of 7.28º, 10.93º, 14.63º, 18.33º, and 22.30º are assigned to the characteristics of the Co-BTC phase observed in the XRD pattern of GCN/Co-BTC [112]. The XRD pattern of GCN/Ni-BTC material shows peaks at 2θ of 7.31º, 10.90º, 13.19º, 14.73º, 16.84º, 18.37º, and 22.51º characteristic of the Ni-BTC phase [113–115]. For GCN/Mn-BTC material, peaks at 2θ of 7.07º, 10.31º, 11.66º, 14.43º, and 20.87º are characteristic of the Mn-BTC phase structure [116–118]. The XRD pattern of GCN/Cr-BTC exhibits characteristic peaks of Cr-BTC at 2θ of 6.49º, 10.96º, 14.80º, 19.10º, 20.15º, 24.31º, and 27.99º [119–121].

The high resolution Fe2p XPS spectra of GCN/Fe-BTC material (Figure 3.4A) show the binding energies of Fe^{2+} (711.15 eV and 723.85 eV), Fe^{3+} (713.39 and 726.00 eV), Fe–N (708.10 eV), and satellite (717.51 and 730.90) [127].

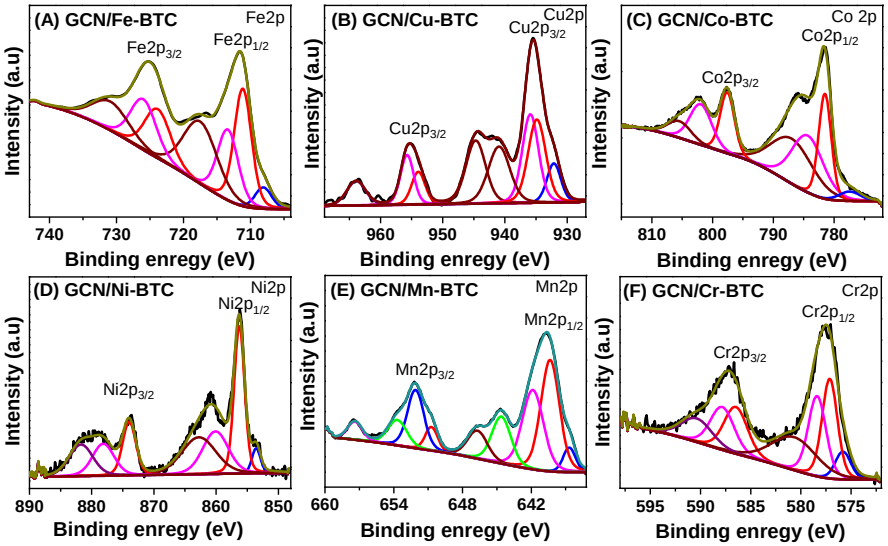

Figure 3.4. High resolution XPS spectra of Fe 2p (A), Cu 2p (B), Co 2p (C), Ni 2p (D), Mn2p (E) and Cr (F) of GCN/Me-BTC material

The high resolution Cu 2p XPS spectra of GCN/Cu-BTC material (Figure 3.4B) exhibit the binding energy peaks of Cu^{+} (934.86 and 953.92

eV), Cu^{2+} (935.91 and 955.72 eV), Cu–N (932.14 eV), and satellite peaks (940.95, 944.69, and 963.91 eV) [109]. The high resolution Co 2p XPS spectra of GCN/Co-BTC material display the binding energy peaks of Co^{2+} (781.51 and 797.58 eV), Co^{3+} (784.35 and 801.95 eV), Co–N (777.41 eV), and satellite (786.97 and 805.47 eV) (Figure 3.4C) [122]. In Figure 3.4D, the binding energies of Ni^{2+} (856.27 and 873.97 eV), Ni^{3+} (860.09 and 878.14 eV), Ni–N (853.56 eV), and satellite (862.77 and 881.72 eV) of GCN/Ni-BTC material [127]. The high resolution Mn 2p XPS spectra of GCN/Mn-BTC material (Figure 3.4E) with the attached binding energy peaks of Mn^{2+} (640.35 and 650.71 eV), Mn^{3+} (641.86 and 652.09 eV), Mn^{4+} (644.61 and 653.69 eV), and Mn–N (638.68 eV). The Cr 2p XPS spectra of GCN/Cr-BTC material reveal the presence of Cr^{2+} (577.13 and 586.48 eV), Cr^{3+} (578.39 and 587.83 eV), Cr–N (575.82 eV), and satellite (580.68 and 590.38 eV) (Figure 3.4F) [45]. The presence of Me^{4+}, Me^{3+}, and Mn^{2+} ions benefits charge separation, efficient charge transfer, and the redox capability of the Me^{3+}/Me^{2+} oxidant pair.

3.1.2. Application of GCN/Me-BTC in tetracycline treatment and CO_2 adsorption

The efficiency of the photocatalytic process of the GCN/Me-BTC photocatalysts is evaluated through the degradation process of TC under visible light irradiation. The removal efficiency of TC in the dark increases in the order of GCN (15.34%) < GCN/Mn-BTC (19.53%) < GCN/Co-BTC (23.02%) < GCN/Ni-BTC (25.69%) < GCN/Cr-BTC (29.86%) < GCN/Fe-BTC (35.98%) < GCN/Cu-BTC (39.05%). Therefore, the TC removal efficiency of GCN/Me-BTC materials is around 15-40% due to the π-π interaction between the benzene ring of TC and the MOF molecule [55]. After 180 minutes of visible light irradiation, the TC removal efficiency at a concentration of 50 mg L^{-1} for GCN (60.88%), GCN/Mn-BTC (69.51%), GCN/Co-BTC (73.12%), GCN/Ni-BTC (78.98%), GCN/Cu-BTC (84.38%), GCN/Cr-BTC (86.12%), and GCN/Fe-BTC (89.57%) is

observed. The TC degradation efficiency of GCN/Mn-BTC, GCN/Co-BTC, and GCN/Ni-BTC materials is slightly higher than GCN due to their higher surface area. These results demonstrate the importance of surface area and pore volume of the materials in the TC treatment.

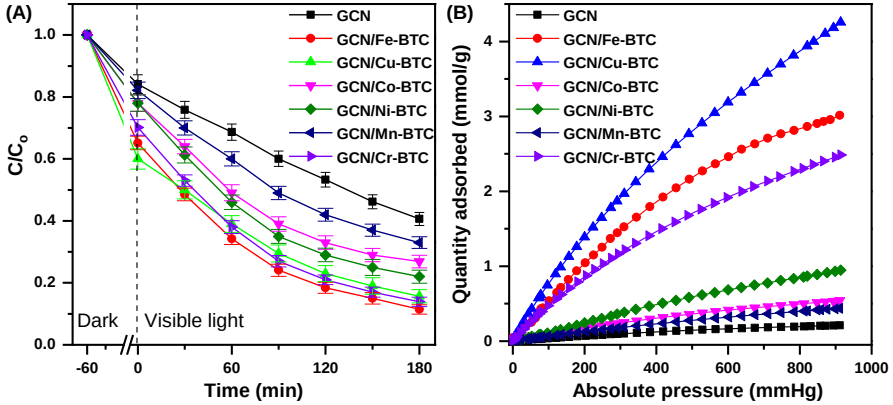

Figure 3.9. (A) TC removal efficiency and (B) CO_2 adsorption capacity of GCN and GCN/Me-BTC materials

(TC concentration: 50 mg L^{-1}; catalyst mass 0.4 g L^{-1}, pH = 6)

The high photocatalytic activity of GCN/Fe-BTC, GCN/Cu-BTC, and GCN/Cr-BTC materials is attributed to several factors: (i) improved light absorption capability, (ii) enhanced charge transfer rate due to the formation of Me-N bonds, (iii) reduced recombination of electrons and holes, (iv) high surface area and large pore volume that facilitate the diffusion rate of reactants. These materials are applied for CO_2 adsorption, as shown in Figure 3.9B. The surface area is directly proportional to the CO_2 adsorption capacity on GCN/Me-BTC materials. Specifically, the CO_2 adsorption capacity decreases in the following order: GCN/Cu-BTC (3.72 mmol g^{-1}) > GCN/Fe-BTC (2.82 mmol g^{-1}) > GCN/Cr-BTC (2.23 mmol g^{-1}) > GCN/Ni-BTC (0.81 mmol g^{-1}) > GCN/Co-BTC (0.47 mmol g^{-1}) > GCN/Mn-BTC (0.38 mmol g^{-1}) > GCN (0.19 mmol g^{-1}). Therefore, GCN/Cu-BTC material exhibits the highest CO_2 adsorption capacity due to

its high surface area, large pore volume, and the proximity of pore diameter to the kinetic diameter of CO_2. Additionally, the addition of GCN reduces the CO_2 adsorption capacity of the material due to the large pore diameter in the layered structure of GCN. This study focuses on synthesizing stable Cu-BTC-II and M-Cu-BTC-II materials in high humidity environments without using harmful organic solvents, reducing crystallization time, and applying them for selective acid gas adsorption.

3.2. Characteristics and applications of GCN/CQD/FeNi-BTC in tetracycline treatment

3.2.1. Characteristic results of GCN/CQD/FeNi-BTC materials

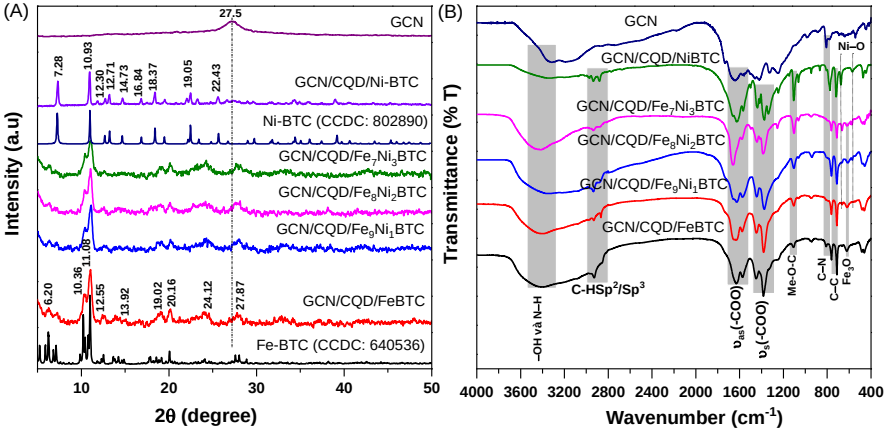

Figure 3.10. (A) XRD patterns and (B) FTIR spectra of GCN, GCN/ CQD/Fe-BTC, GCN/CQD/Ni-BTC and GCN/CQD/FeNi-BTC materials

The GCN/CQD/Fe-BTC shows peaks at 2θ of 6.20º, 10.36º, 11.08º, 12.55º, 13.92º, 19.02º, 20.16º, 24.12º, and 27.87º characteristic of the Fe-BTC phase [108]. The GCN/CQD/FeNi-BTC material has characteristic peaks of Ni-BTC with very low intensity, possibly due to overlapping with the peaks of the Fe-BTC phase and the even dispersion within the Fe-BTC framework. Additionally, the GCN/ CQD/Fe-BTC, GCN/CQD/Ni-BTC, and GCN/CQD/FeNi-BTC materials do not show the characteristic peak at 2θ of 27.5º the GCN phase, which may be due to overlapping with the

peaks of the FeNi-BTC phase and the layered structure of the GCN material helping to evenly disperse the Me-BTC nano particles (Ni-BTC and Fe-BTC) on the surface of GCN [122].

3.2.2. Application of GCN/CQD/FeNi-BTC in tetracycline treatment

GCN/CQD/Ni-BTC, GCN/CQD/FeBTC, and GCN/CQD/FeNi-BTC materials were evaluated for catalytic activity in the process of treating the antibiotic tetracycline. The GCN/CQD/Fe-BTC and GCN/CQD/FeNi-BTC materials showed effective TC adsorption ranging from 30.22 to 46.13% after 60 minutes (Figure 3.19A). During the photocatalytic process, after 90 minutes of light irradiation, the TC treatment efficiency was observed to reach 65.18, 90.43, 93.54, 96.28, 93.75 and 86.26% respectively for GCN, GCN/CQD/Fe-BTC, GCN/CQD/Fe_9Ni_1BTC, GCN/CQD/Fe_8Ni_2BTC, GCN /CQD/Fe_7Ni_3BTC, and GCN/CQD/Ni-BTC. The GCN/CQD/FeNiBTC materials exhibited superior TC degradation efficiency compared to GCN due to the simultaneous integration of active phases through the CQD bridge, enhancing charge separation efficiency, preventing recombination of electrons and holes, and facilitating electron transfer. These results were confirmed through UV-Vis DRS, PL, and EIS methods (Figure 3.17).

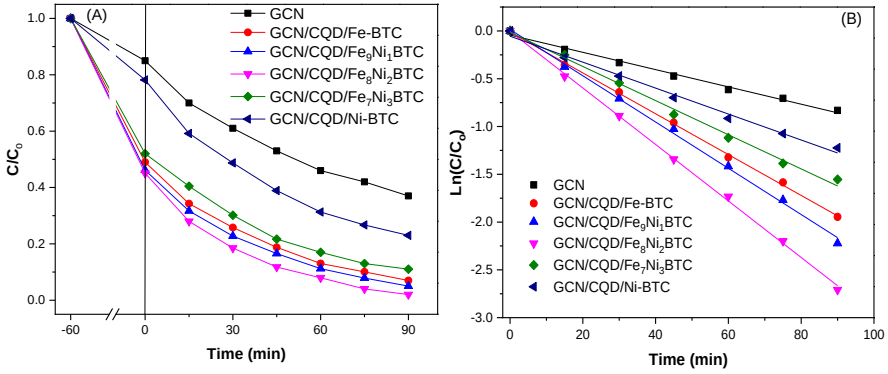

Figure 3.19. C/C_o functions of reaction time (A) and first-order kinetics (B) of GCN/CQD/Fe-BTC and GCN/CQD/FeNi-BTC materials

3.3. The Ag_3PO_4/GCN/FeNi-BTC/CQD (AGF-CQD) materials

3.3.1. Characteristics of the AGF-CQD material

The XRD pattern of the Ag_3PO_4, FeNi-BTC, GCN, and AGF-CQD materials is presented in Figure 3.20A. The XRD pattern of the GCN material shows a broad peak at 2θ of 27.5° (002) characteristic of GCN [142]. The peaks at 2θ of 20.92° (110), 29.72° (200), 33.36° (210), 36.61° (211), 42.55° (220), and 47.86° (310) are characteristic of the Ag_3PO_4 phase [143]. The FeNi-BTC material exhibits peaks at 2θ of 6.20°, 10.42°, 11.09°, 12.6°, 19.02°, 20.05°, and 27.83° [122]. In the XRD pattern of the AGF-CQD material, all characteristic peaks of the Ag_3PO_4 and FeNi-BTC phases are observed. However, the characteristic peak of GCN is not clearly visible, possibly due to overlapping with the peaks of the FeNi-BTC phase [142]. The intensity of the characteristic peaks of Ag_3PO_4 significantly increases as the Ag_3PO_4 content increases from 0 to 30 wt%.

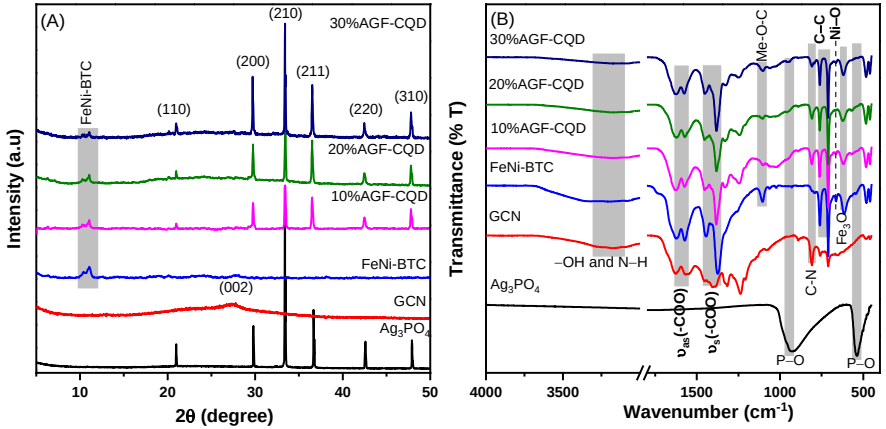

Figure 3.20. (A) XRD patterns and (B) FTIR spectra of Ag_3PO_4, FeNi-BTC, GCN and AGF-CQD materials

Mott-Schottky plots are used to determine the flat band potential (E_{fb}) of the Ag_3PO_4, GCN, and FeNi-BTC materials. Figure 3.30 confirms that the Ag_3PO_4, GCN, and FeNi-BTC materials are all n-type semiconductors, as they exhibit negative slope, consistent with the report by Xi Rao and et al.

[149]. The flat band potentials of the Ag_3PO_4, GCN, and FeNi-BTC materials are –0.26, –1.36, and –0.45, respectively. The flat band potential on the Ag/AgCl electrode can be compared to the normal hydrogen electrode (NHE) based on equation (3.1)

$$E_{(NHE)} = E^{o}_{Ag/AgCl} + E_{Ag/AgCl} + 0.059pH \quad (3.1)$$

where $E^{o}_{Ag/AgCl}$ = 0.1976 eV at 25 ◦C and $E_{Ag/AgCl}$ is the working potential using Ag/AgCl (pH of 7.4)

The flatband potentials (E_{fb}) of Ag_3PO_4, FeNiBTC, and GCN are determined according to equation (3.1) to be +0.37, +0.18, and –0.73 eV versus NHE, respectively. The valence band (VB) of n-type semiconductor materials with a flatband width (E_{fb}) ranging from 0.1 to 0.2 is chosen to be 0.2 eV. Therefore, the VB values of Ag_3PO_4, FeNiBTC, and GCN materials are 0.17, –0.02, and –0.93 eV, respectively. The CB values of Ag_3PO_4, FeNiBTC, and GCN can be calculated based on the relationship between Eg and E_{VB} potentials, which are 2.52, 2.69, and 1.81 eV, respectively.

3.3.2. Efficiency of photocatalytic treatment of Fe-NiBTC, 20%AGF, and AGF-CQD catalysts

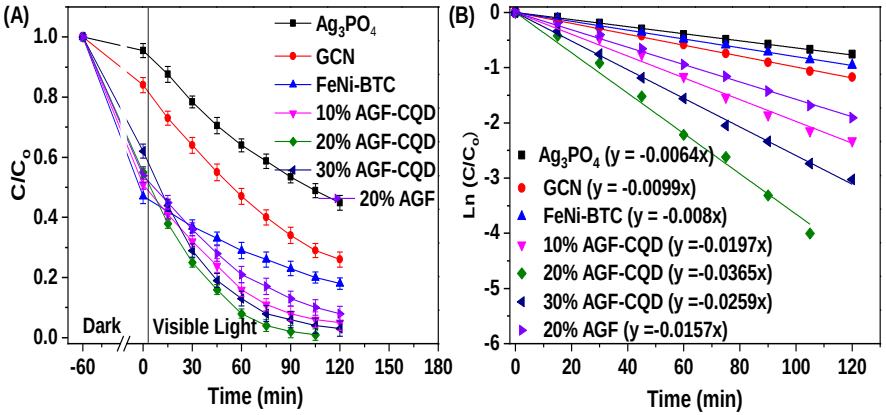

Figure 3.31. (A) C/C_o versus reaction time and (B) first-order reaction kinetics on Ag_3PO_4, GCN, FeNi-BTC, 20%AGF and AGF-CQD materials.

The catalytic efficiency of Ag_3PO_4, GCN, Fe-NiBTC, 20%AGF, and AGF-CQD materials in the degradation process of tetracycline antibiotics has been evaluated.

3.3.4. The mechanism of electron separation and the formation of reaction radicals

To better understand the photocatalytic mechanism of the AGF-CQD photocatalyst in the tetracycline treatment process, trapping experiments of active radicals were conducted in Figure 3.34. In Figure 3.34A, the tetracycline treatment efficiency of the AGF-CQD photocatalyst reached 62.23% when p-BQ was added to trap the $^{\bullet}O_2^-$ radicals. When BQ, AO, and TBA were successively added to the reaction system, the tetracycline treatment efficiency was 72.56%, 76.34%, and 93.92% after 60 minutes of visible light irradiation. Therefore, the roles of reaction radicals in the tetracycline antibiotic degradation process are in the order of $^{\bullet}O_2^-$ > h^+ > $^{\bullet}OH$.

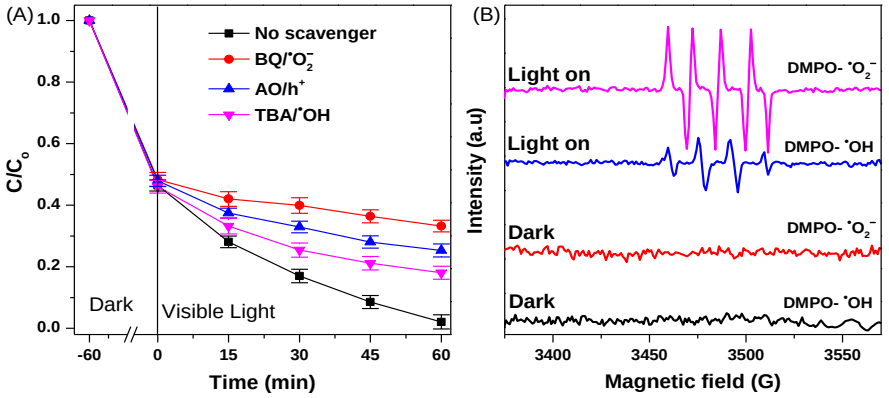

Figure 3.34. (A) Reactive radical trapping experiments and (B) EPR spectrum to detect $^{\bullet}OH$ and $^{\bullet}O_2^-$ onver 20%AGF-CQD.

Electron spin resonance (ESR) was conducted using DMPO as an electron trap to identify the $^{\bullet}O_2^-$ and $^{\bullet}OH$ reaction radicals. In Figure 3.34B, the signal intensity ratio was observed to be 1:2:2:1 for DMPO–$^{\bullet}OH$ and

the characteristic intensity ratio was 1:1:1:1 for DMPO–$^{\bullet}O_2^-$ when exposed to visible light [108]. In Figure 3.35A, the conduction band energy (CB) of Ag_3PO_4 (0.17 eV) and FeNi-BTC (–0.02 eV) has a more positive reduction potential than Eo $O_2/^{\bullet}O_2^-$=–0.33 eV, leading to the formation of $^{\bullet}O_2^-$ radicals being unfeasible in these two semiconductors [108]. On the contrary, ECB of GCN (–0.93 eV) shows a more negative reduction potential than E^o $O_2/^{\bullet}O_2^-$ = –0.33 eV, allowing the formation of $^{\bullet}O_2^-$ radicals in the CB of GCN [162]. Figure 3.35. Schematic diagram of charge separation and transfer process of 20%AGF-CQD material before and after contact. In the valence band (ECB), GCN (1.81 eV) has a lower energy than the oxidation potential of E° $H_2O/^{\bullet}OH$ ($h^+ + H_2O \rightarrow {}^{\bullet}OH$, E° $H_2O/^{\bullet}OH$ = 2.40 eV), thus preventing the formation of $^{\bullet}OH$ radicals in the CB of GCN. Conversely, due to the high valence band energy of Ag_3PO_4 (2.52 eV) and FeNi-BTC (2.65 eV) compared to the oxidation potential of E° $H_2O/^{\bullet}OH$ ($h^+ + H_2O \rightarrow {}^{\bullet}OH$, E° $H_2O/^{\bullet}OH$ = 2.40 eV), $^{\bullet}OH$ radicals can be generated in the CB of Ag_3PO_4 and FeNi-BTC. Based on the electrochemical properties and the role of reactive radicals, the thesis proposed the band structure of AGF-CQD material (Figure 3.35B).

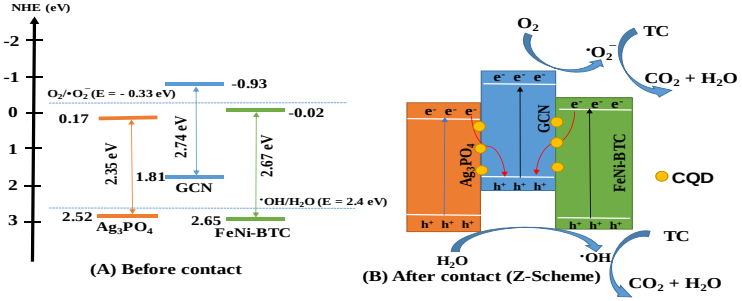

Figure 3.35. Scematic illustration of separation and photo charge transfer on 20%AGF-CQD sample before and after contact.

First, the electron holes (h^+) and electrons (e^-) are excited by a light source with energy greater than 2.64 eV (Equation (3.3)). Then, the electrons are separated and move to the conduction band (CB) and react

with O_2 to form $^{\bullet}O_2^-$ radicals (Equation (3.4)). The strong connection between semiconductors through the formation of Me-N bonds and tight bonding by CQD in AGF-CQD, electrons in the conduction band of Ag_3PO_4 and FeNi-BTC can easily move and recombine with the electron holes (h^+) in the valence band of GCN (Ag_3PO_4 → CQD → GCN and FeNi-BTC → CQD → GCN), (Equation (3.5)). Next, under the influence of visible light, electrons (e^-) and holes (h^+) continue to separate to react with O_2 to create $^{\bullet}O_2^-$ radicals (Equation (3.4)). In the valence band (VB), the valence band energy of Ag_3PO_4 (2.52 eV) and FeNi-BTC (2.65 eV) is higher than the energy of $H_2O/^{\bullet}OH$ (2.40 eV), so h^+ reacts with –OH or H_2O absorbed on the surface to generate $^{\bullet}OH$ radicals (Equation 3.6).

$$Ag_3PO_4/GCN/FeNi\text{-}BTC/CQD + hv \rightarrow holes\ (h^+)\ and\ electrons\ (e^-) \quad (3.3)$$

$$O_2 + GCN\ (e^-) \rightarrow {}^{\bullet}O_2^- \quad (3.4)$$

$$Ag_3PO_4(e^-) + FeNi\text{-}BTC(e^-) + GCN(h^+) \rightarrow GCN\ (e^- + h^+) \quad (3.5)$$

$$Ag_3PO_4(h+) + FeNi\text{-}BTC(h^+) + –OH\ \text{ or } H_2O \rightarrow {}^{\bullet}OH \quad (3.6)$$

Finally, the formed reaction radicals such as $^{\bullet}OH$, $^{\bullet}O_2^-$, and h^+ oxidize tetracycline into less toxic products.

3.4. The Cu-BTC-II material is used as an adsorbent for acidic gases (CO_2 and H_2S)

Cu-BTC-II material is synthesized using a hydrothermal method combined with microwave under different synthesis conditions, including hydrothermal microwave time, temperature, and solvent amount. The research results show that the reaction time, temperature, and amount of organic solvent (isopropanol, imidazole) affect the synthesis process of Cu-BTC-II using the hydrothermal microwave method. This study has provided optimal synthesis conditions for M-Cu-BTC-II, such as a hydrothermal microwave support time of 30 minutes, a temperature of 100 ^oC, and a water-repellent solvent amount of isopropanol (3 mL), imidazole (4 mmol). Based on this, the study used the optimal process to investigate the influence of various metal ions.

3.5. The M-Cu-BTC-II material used as an adsorbent for acidic gases (CO_2 and H_2S).

3.5.1. The characteristic results of Cu-BTC-II and M-Cu-BTC-II materials

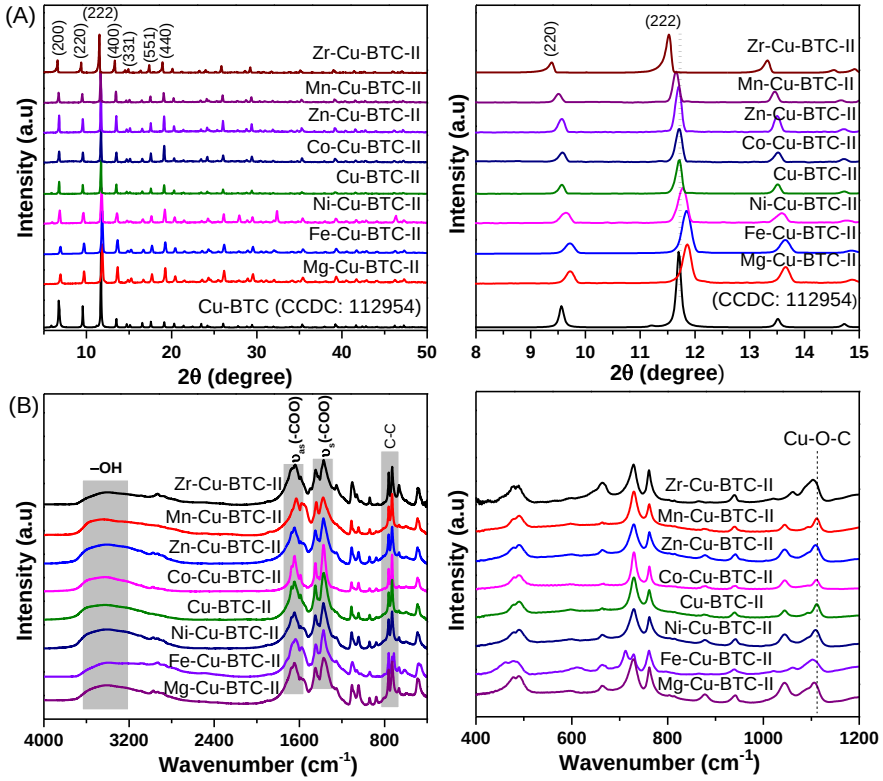

Figure 3.51. (A) XRD pattern and (B) FTIR spectrum of Cu-BTC-II and M-Cu-BTC-II

Figure 3.51 XRD pattern of Cu-BTC-II and M-Cu-BTC-II materials synthesized by hydrothermal method with microwave assistance showed peaks at 2θ of 7.0° (200), 9.71° (220), 11.83° (222), 13.6° (400), 15.3° (331), 16.6° (422), 17.7° (511), and 19.3° (440) characteristic of Cu-BTC material (CCDC: 112954). These results indicate that the modification of Cu-BTC with isopropanol and imidazole does not affect the crystal growth of Cu-BTC during synthesis. When Ni, Fe, and Mg ions are introduced as

second metal cations, the diffraction angles of Cu-BTC-II structure shift towards larger 2θ angles (Figure 3.51A).

This can be explained by the smaller ionic radii of Mg^{2+} (0.65 Å), Fe^{2+} (0.64 Å), and Ni^{2+} (0.69 Å) compared to Cu^{2+} (0.72 Å), resulting in the contraction of the Cu-BTC crystal lattice [167]. On the other hand, Zn-Cu-BTC-II, Mn-Cu-BTC-II, and Zr-Cu-BTC-II have diffraction angles shifted to lower positions, due to the larger ionic radii of Zn^{2+} (0.74 Å), Mn^{2+} (0.80 Å), and Zr^{4+} (0.82 Å) compared to Cu^{2+} (Table 3.15).

3.5.1.3. N_2 adsorption-desorption isotherms of M-Cu-BTC-II

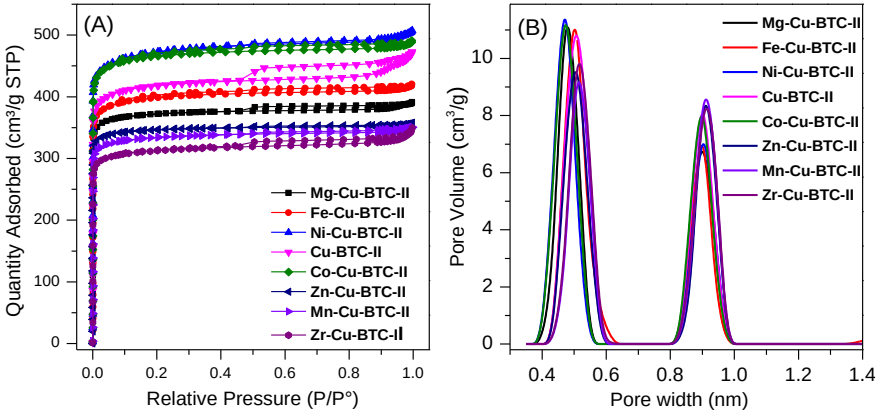

Figure 3.55. N_2 adsorption-desorption isotherms (A) and DFT pore size distribution curve of Cu-BTC-II and M-Cu-BTC-II materials

DFT and BET equations are used to evaluate the pore size distribution and surface area of Cu-BTC-II and M-Cu-BTC-II materials by examining the N_2 adsorption-desorption isotherms at 77 K (Figure 3.55). All Cu-BTC-II and M-Cu-BTC-II materials exhibit type I isotherms with H4 hysteresis classified by IUPAC [172]. The N_2 adsorption isotherms of all materials show rapid N_2 uptake at relatively low pressure ($P/P_0 < 0.1$), indicating the presence of mostly microporous structures [173]. In Table 3.18, the Brunauer – Emmett – Teller (BET) surface area of Cu-BTC is 1659 $m^2\ g^{-1}$ and the pore volume is 0.723 $cm^3\ g^{-1}$. It is noteworthy that the surface area

and pore volume of Cu-BTC-II materials containing Co and Ni both slightly increase, while the surface area of Fe-Cu-BTC-II and Mn-Cu-BTC-II samples tend to decrease.

3.4.1.6. Surface properties and acid-base

Electrostatic interactions play an important role in the adsorption process of H_2S and CO_2, so the zeta potential method has been used to evaluate the surface charge of materials. Figure 3.58, the Cu-BTC-II material shows a zeta potential of +13.54 mV, indicating that this material has a positive charge [178], consistent with the report by Li et al [179].

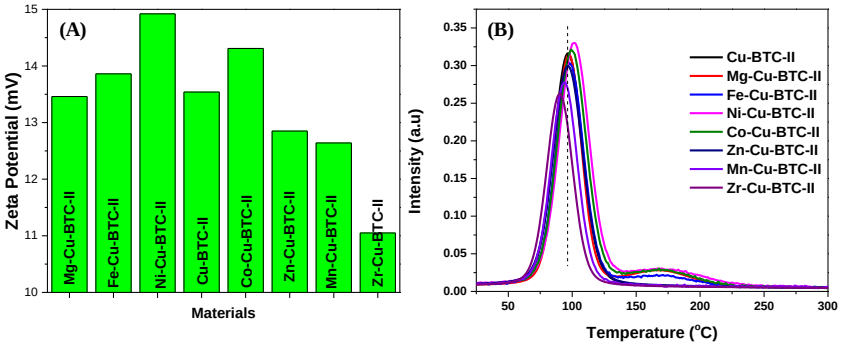

Figure 3.56. (A) Zeta potential and (B) CO_2-TPD of the M-Cu-BTC-II materials

M-Cu-BTC-II, combining Zr, Mn, Zn, and Mg lead to a decrease in the zeta potential of Cu-BTC-II, while the addition of Ni, Co, and Fe to the structure results in an increase in the positive charge of the Cu-BTC-II material. Therefore, Ni-Cu-BTC-II, Co-Cu-BTC-II, and Fe-Cu-BTC-II materials are expected to have stronger electrostatic interactions with CO_2 and H_2S [180]. The acid-base properties of Cu-BTC-II and M-Cu-BTC-II have been analyzed using CO_2 temperature-programmed desorption (CO_2-TPD) from 30 to 300 °C. The Cu-BTC-II material shows a CO_2 desorption peak at 98 °C, indicating weak interaction with CO_2 [181]. For Zr-Cu-BTC-II, Zn-Cu-BTC-II, and Mn-Cu-BTC-II, this desorption peak shifts slightly to 90–94.5 °C with lower intensity compared to Cu-BTC-II, indicating a decrease in the interaction between the material and CO_2 due to electrostatic interaction and decreased specific surface area. Meanwhile, Mg-Cu-BTC-II, Fe-Cu-BTC-II, Ni-Cu-BTC-II, and Co-Cu-BTC-II exhibit

a high intensity desorption peak at 100 °C and a weaker peak at 160–170 °C, showing a stronger interaction of the Fe, Ni, Co, Mg centers with CO_2. These results confirm the presence of stronger adsorption centers in Mg-Cu-BTC-II, Fe-Cu-BTC-II, Ni-Cu-BTC-II, and Co-Cu-BTC-II compared to Cu-BTC-II [181–183].

3.5.2. Adsorption of H_2S, CO_2, N_2 and CH_4 on M-Cu-BTC-II

The ability to adsorb H_2S, CO_2, CH_4, and N_2 of Cu-BTC-II and M-Cu-BTC-II is carried out at 20 °C and 1 atm.

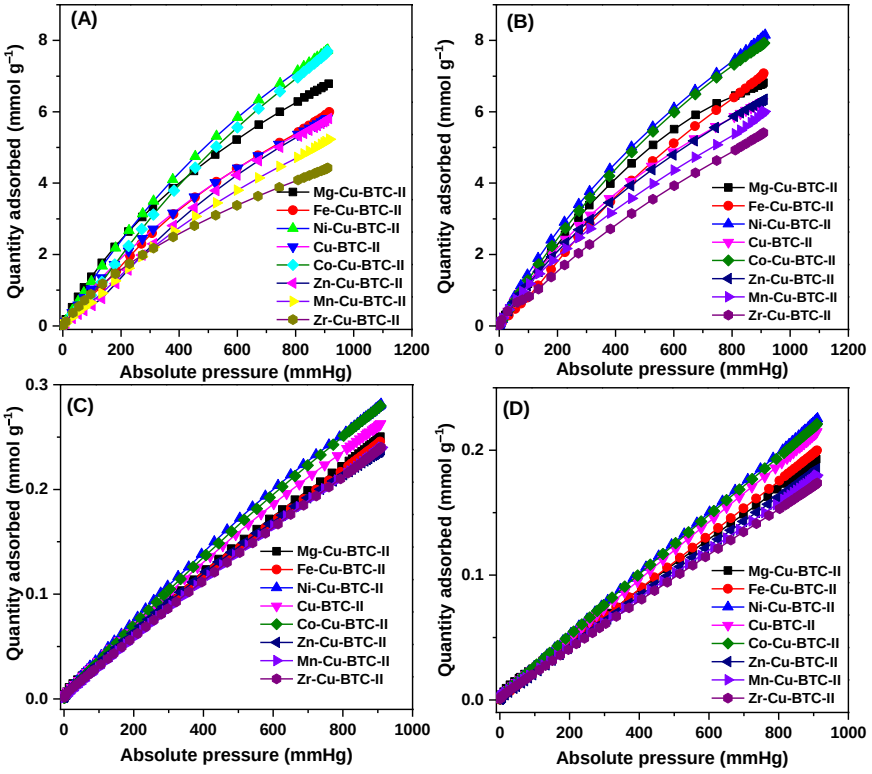

Figure 3.59. Adsorption isotherms of CO_2 (A), H_2S (B), CH_4 (C) and N_2 (D) of Cu-BTC-II and M−Cu−BTC−II at 20 °C and 1 atm.

Figure 3.59 shows the adsorption capacity of Cu-BTC-II for N_2 (0.15 mmol g^{-1}) < CH_4 (0.20 mmol g^{-1}) < CO_2 (5.16 mmol g^{-1}) < H_2S (5.66 mmol g^{-1}). The adsorption capacity of Cu-BTC-II material is high for CO_2

and H_2S due to its large surface area (1659 m^2 g^{-1}, Table 3.18) and appropriate pore size (5.1 Å, Table 3.18) for selective adsorption of H_2S and CO_2 [86,185]. The higher adsorption capacity for H_2S compared to CO_2 may be due to the fact that H_2S (3.6×10^{-24} cm^3) is more polar than CO_2 molecules (2.9×10^{-24} cm^3) [186]. Therefore, H_2S interacts more easily with the heterogeneous surface of Cu-BTC-II. For gases CH_4 and N_2, their molecular structures are symmetrical and non-polar, leading to weaker interactions of CH_4 and N_2 with the surface of Cu-BTC-II compared to the interactions of H_2S and CO_2, resulting in lower adsorption capacity (Figure 3.59C-D). This is supported by the fact that the polarity of CH_4 (2.6×10^{-24} cm^3) and N_2 (1.76×10^{-24} cm^3) is lower than that of H_2S and CO_2 [187]. When Ni^{2+} and Co^{2+} ions are introduced as the second metal cations in Cu-BTC-II to form Ni-Cu-BTC-II and Co-Cu-BTC-II, the adsorption capacity for H_2S significantly increases from 5.66 mmol g-1 to 7.16 and 7.04 mmol g^{-1} (Figure 3.59B). This significant increase is due to the dual metal ion M-Cu-BTC-II (M=Ni or Co) with smaller pore diameters (<7 Å) compared to Cu-BTC-II (7.23 Å), leading to thermodynamically favorable conditions for the H_2S adsorption process at ambient pressure [174], as well as the cooperative effect of metal ions on the same network node [188]. Furthermore, the increased surface charge and stronger activity of the basic sites also enhance the electrostatic interaction between the metal ions in M-Cu-BTC-II (M=Ni or Co) with acid gases (CO_2 and H_2S) (Figure 3.58). Conversely, Zn-Cu-BTC-II, Mn-Cu-BTC-II, and Zr-Cu-BTC-II have reduced CO_2 and H_2S adsorption capacities compared to Cu-BTC (Figure 3.59A and B), due to decreased surface charge, surface area, pore volume, and increased pore diameter (Table 3.18) leading to a decrease in the electrostatic interaction of the material with acid gases. Therefore, Mao quản with a diameter smaller than 7 Å will benefit the selective adsorption ability of H_2S and CO_2 gas molecules at low pressure (<1.0 MPa) [185]. Additionally, Cu-BTC-II and M-Cu-BTC-II can bond with H_2S to form O-

Cu-S chemical bonds due to the free electron pair in S with the third electron of Cu ion [189]. Moreover, the interaction between Cu^{2+} and S atoms in H_2S through chemical bonding (chemical adsorption) is the main interaction between H_2S molecules and M-Cu-BTC-II, helping to increase the adsorption capacity of H_2S [189]. Figures 3.59C and D show that the larger the surface area and pore volume of mao quản, the higher the adsorption capacity of CH_4 and N_2 gas (Table 3.18), this is due to the pore filling adsorption mechanism for N_2 and CH_4 gas.

3.5.8. The recyclability of Ni-Cu-BTC-II

The good adsorption material is not only a material with high adsorption capacity but also can be regenerated and used for many different adsorption-desorption cycles. To study the durability of Ni-Cu-BTC-II, the material that has been used is regenerated by Ar at 120 °C for 5 hours per cycle [214]. Figure 3.71B, Ni-Cu-BTC-II can be reused at least 10 times without significantly reducing the adsorption capacity, decreasing from 6.87 to 5.85 mmol g^{-1} after 10 cycles.

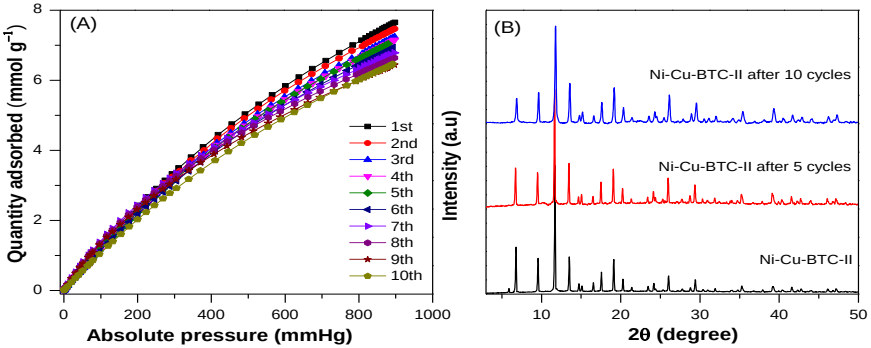

Figure 3.71. (A) CO_2 adsorption isotherms at different adsorption cycles and (B) XRD pattern of Ni-Cu-BTC-II before and after CO_2 adsorption cycles

CONCLUSION

From the research results of the thesis, the author draws the following conclusions:

1. Successfully synthesized GCN/Me-BTC (Me: Fe, Cu, Co, Ni, Mn, Cr), GCN/FeNi-BTC/CQD, Ag_3PO_4/GCN/FeNi-BTC/CQD, and M-Cu-BTC-II (M: Mg, Fe, Ni, Co, Zn, Mn, Zr, and Zr; II = isopropanol and imidazole) materials using the hydrothermal microwave-assisted method for 30 minutes without using harmful organic solvents. The GCN/FeNi-BTC/CQD and Ag_3PO_4/GCN/FeNi-BTC/CQD (AGF-CQD) materials possess many outstanding advantages such as (i) high surface area, (ii) strong visible light absorption and bandgap energy of 2.28–2.63 eV, (iii) efficient separation of electrons and holes, (iv) improved electron diffusion and transfer, (v) reduced recombination ability of photogenerated holes and electrons, (vi) small particle size of 20-50 nm. The M-Cu-BTC-II material has particle sizes of 20–30 µm, surface areas of 1259–1877 $m^2\ g^{-1}$, pore volumes of 0.409–0.609 $cm^3\ g^{-1}$, and features tetrahedral 5Å and square channels 9Å

2. The 20% Ag_3PO_4/GCN/FeNi-BTC material integrated with quantum dot carbon dots enhances the contact between the reaction phases, leading to superior TC treatment efficiency, reaching 98.4% after 60 minutes of reaction, with a TC concentration of 30 mg L^{-1}. Under optimal experimental conditions ([photocatalyst] = 0.4 g L^{-1}, [TC] = 30 mg L^{-1}, irradiation power of 300 W, and pH = 6), the 20% AGF-CQD material achieves a tetracycline removal efficiency of 98.4% after 60 minutes of visible light irradiation.

3. The Ag_3PO_4/GCN/FeNi-BTC/CQD photocatalyst separates electrons and forms reaction radicals according to the Z-scheme mechanism. The roles of the reaction radicals in the TC degradation process in the order $^{\bullet}O_2^-$ > h^+ > $^{\bullet}OH$ are confirmed by radical trapping experiments and ERS spectroscopy.

4. The Ni-Cu-BTC-II material has CO_2 and H_2S adsorption capacities of 5.91 and 5.84 mmol g^{-1} respectively under environmental conditions (25 °C and 1 atm) and remains stable over 10 CO_2 adsorption cycles. The high gas adsorption capacity of Ni-Cu-BTC-II is due to its high surface area, large pore volume, and pore size consisting of tetrahedral channels (5 Å) and square channels (9 Å) that are very suitable for adsorbing acid gases under environmental conditions (25 °C and 1 atm). The Ni-Cu-BTC-II material exhibits structural stability in humid environments or acidic environments (pH = 3) compared to the Ni-Cu-BTC material that was not functionalized with isopropanol and imidazole. The process of acid gas adsorption (CO_2 and H_2S) begins with electrostatic interactions and plays a crucial role in the acid gas adsorption process. In the H_2S adsorption process, in addition to electrostatic interactions, the chemical bonding between M ions (Cu^{2+} and Ni^{2+}) and S atoms in H_2S also significantly contributes to enhancing the efficiency of H_2S adsorption.

NEW CONTRIBUTIONS OF THE THESIS

1. Synthesized of GCN/Me-BTC materials (Me: Fe, Cu, Co, Ni, Mn, Cr), GCN/FeNi-BTC/CQD, Ag_3PO_4/GCN/FeNi-BTC/CQD, and M-Cu-BTC-II (M: Mg, Fe, Ni, Co, Zn, Mn, Zr, and Zr; II = isopropanol and imidazole) was successfully achieved using the hydrothermal microwave-assisted method without the use of harmful organic solvents.

2. The formation mechanism of the reaction centers of three photo-catalysts Z-scheme including GCN/Me-BTC, GCN/FeNi-BTC/CQD, and Ag_3PO_4/GCN/FeNi-BTC/CQD has been identified through a combination of radical trapping experiments, XPS, and EPR methods. The formation of Me–N covalent bonds and integration with carbon quantum dots (CQD) enhances interfacial contact between semiconductors, leading to increased electrical conductivity, enhanced light absorption capacity, and reduced recombination of electron-hole pairs.

3. The Ni-Cu-BTC-II material has CO_2 and H_2S adsorption capacities of 5.91 and 5.84 mmol g^{-1} respectively under ambient conditions (25 °C and 1 atm) and remains stable for 10 CO_2 adsorption cycles. Electrostatic interaction plays an important role in the gas adsorption process (CO_2 and H_2S) on the Ni-Cu-BTC-II adsorbent. Additionally, the chemical bonding between M ions (Cu^{2+} and Ni^{2+}) and S atoms in H_2S also significantly contributes to enhancing the H_2S adsorption efficiency of M-Cu-BTC-II

LIST OF THE PUBLICATIONS RELATED TO THE DISSERTATION

1. **Manh B. Nguyen,** Linh Ho Thuy Nguyen, Hoa Thi Lai, Huan V. Doan, Ngoc Quang Tran, Ngoc Xuan Dat Mai, Lam Dai Tran, Philip Anggo Krisbiantoro, Kevin C.-W. Wu, Tan Le Hoang Doan, Tuning the composition of highly stable mixed-metal MOFs by microwave-assisted hydrothermal method for ultra-high selective and simultaneous capture of CO_2 and H_2S, *Chemical Engineering Journal*, 497, 2024, 154479 (Q1, IF 13.2).

2. Hoa T Vu, Giang TT Pham, Tan Le Hoang Doan, Tran Dai Lam, Ngo Thuy Van, Nguyen Van Manh, Pham Thi Quyen, Nguyen Duc Hai, Huan V Doan, **Manh B Nguyen***, Influence of metal ions (Me: Fe, Cu, Co, Ni, Mn, Cr) on direct Z-scheme photocatalysts CN/Me-BTC on the degradation efficiency of tetracycline in water environment, *Journal of the Taiwan Institute of Chemical Engineers*, 161, 2024, 105518 (Q1, IF 6.3).

3. **Manh B. Nguyen**, Huan V. Doan, Doan Le Hoang Tan, Tran Dai Lam, Advanced g-C_3N_4 and bimetallic FeNi-BTC integration with carbon quantum dots for removal of microplastics and antibiotics in aqueous environments, *Journal of Environmental Chemical Engineering*, 12, 3, 2024, 112965 (Q1, IF 7.2).

4. **Manh B. Nguyen**, Huan V. Doan, Doan Le Hoang Tan, Tran Dai Lam, Enhancement of tetracycline photocatalytic degradation under visible light: Unleashing the synergy of Z-scheme Ag_3PO_4/GCN/FeNi-BTC photocatalyst with carbon quantum dots, *Journal of Industrial and Engineering Chemistry*, 141, 2025, 380-393 (Q1, IF 6.0).